

Identification of the transition state for fast reactions: The trapping of hydroxyl and methyl radicals by DMPO—A DFT approach

Benjamín Aguilera-Venegas ^{a,b,*}, Hernán Speisky ^{a,c}



^a Laboratory of Antioxidants, Institute of Nutrition and Food Technology, University of Chile, Av. Macul 5540, P.O. Box 138-11, Santiago, Chile

^b Department of Inorganic and Analytical Chemistry, University of Chile, Box 233, Santiago, Chile

^c Department of Chemical Pharmacology and Toxicology, Faculty of Chemical and Pharmaceutical Sciences, University of Chile, Box 233, Santiago, Chile

ARTICLE INFO

Article history:

Accepted 17 June 2014

Available online 24 June 2014

Keywords:

Density functional theory
Spin-trapping
Free radical

DMPO

Hydroxyl and methyl radicals
Electron spin resonance

ABSTRACT

Up to date, attempts to locate the transition state (TS) for the trapping reaction between $\cdot\text{OH}$ and DMPO have been unsuccessful, and the lack of molecular mechanisms by which $\cdot\text{OH}$ binds to the spin-trap constitutes a question still unsolved. Herein, we have taken a step forward on this task by describing the theoretical TS for the trapping of $\cdot\text{OH}$ and $\cdot\text{CH}_3$ by DMPO and the intrinsic reaction coordinates. This work aims to provide new understandings on the molecular orbital (MO) interactions that rule these reaction paths. Besides we assessed the degree of involvement of weak interactions and the charge transfer (CT) phenomenon involved in such interactions. Regarding the trapping of $\cdot\text{OH}$, the beginning of the reaction would be ruled by weak interactions to then give way to stronger MO interactions conducive to the formation of the TS. For $\cdot\text{CH}_3$, the reaction is, instead, early ruled by significant MO interactions, and a relatively small contribution in the weak interactions range. At the TS, both reactions share the formation of an antibonding orbital responsible for hosting the unpaired electron, and two bonding orbitals between the radical and the spin-trap. Additionally, the charge is transferred primarily from DMPO to $\cdot\text{OH}$ through β orbitals, while for $\cdot\text{CH}_3$, the CT occurs in both directions, so that while DMPO behaves like an α -acceptor/ β -donor, $\cdot\text{CH}_3$ acts as a β -acceptor/ α -donor. Finally, we provide evidence showing that the resultant theoretical models are in agreement with the hyperfine coupling constants as obtained from biological-ESR spin trapping experiments.

© 2014 Elsevier Inc. All rights reserved.

1. Introduction

The continuous disruption of redox signaling processes by free radicals often leads to uncontrolled alterations in the redox status of cells which, ultimately, either trigger and/or accelerate the development of a various oxidation-related human pathologies (e.g. some tumoral, cardiovascular and neurodegenerative diseases). Oxidative alterations, however, can also become a pharmacological tool for the treatment of certain pathologies, such as it occurs in parasitic diseases, and certain forms of cancers [1,2]. Consequently, the accurate detection and quantification of free radicals in biological systems is a relevant issue in the search of new targeted drugs. There are several ways to assess the progress of the free radicals production along a biological reaction. One of them, is by means of ESR-based techniques which, besides providing an

overview about the production of free radicals, allows the identification of very short-lived radicals (e.g. $\cdot\text{OH}$, $\text{O}_2^{\bullet-}$) by means of their characteristic and easily recognizable ESR spectrum and hyperfine coupling constants (HFCCs). In the spin-trapping technique, a spin-trap molecule reacts with a short-lived radical leading to the formation of a spin-adduct, a “more stable radical” which exhibits a longer half-life than the isolated radical [3]. Thus, the spin-trapping technique offers a practical form to establish what kind of radical can be generated by recently synthesized ROS-producing drugs [4]. However, whenever the HFCCs are the only parameters under determination, the electronic/molecular structures of the spin-adduct cannot be categorically established [5], and therefore, an interpretation solely based on HFCCs data can eventually lead to misleading conclusions [6].

Up to date, a variety of spin-trapping reactions have been theoretically addressed. Among these are the reactions between methyl, superoxide, hydroxyl, hydroperoxy and nitric oxide radicals alongside several spin-traps [7–10]. Most studies conducted so far have focused their attention on discussing prediction of thermodynamic parameters, decay pathways, and rate constants [11]. However, the process by which the radical and the spin-trap interact to give rise

* Corresponding author at: Laboratory of Antioxidants, Institute of Nutrition and Food Technology, University of Chile, Av. Macul 5540, P.O. Box 138-11, Santiago, Chile. Tel.: +56 2 29782963; fax: +56 2 27370567.

E-mail address: benya@ciq.uchile.cl (B. Aguilera-Venegas).

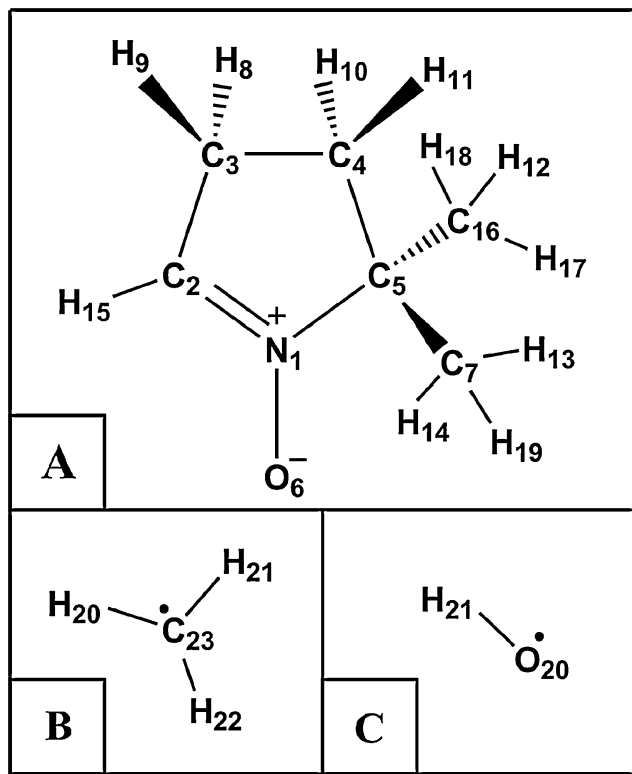


Fig. 1. Arbitrary numbering of the atoms involved in the reactions here investigated. (A) DMPO, (B) methyl radical and (C) hydroxyl radical.

to a binding interaction constitutes a largely unsolved issue. In fact, attempts to locate the transition state (TS) for the trapping reaction between $\cdot\text{OH}$ and DMPO (5,5-dimethyl-1-pyrroline-N-oxide) have been unsuccessful, thus leaving a void in current knowledge on this type of reactions, so far, limited to the understanding of the independent states, i.e. reactants and products [9]. Thus, in order to fill the above-referred void, the present work aims to provide an accurate picture of the entrapment reactions between some biologically relevant radicals ($\cdot\text{OH}$ and $\cdot\text{CH}_3$) and DMPO (Fig. 1).

These radicals were chosen mainly due to their biological implications. Thus, $\cdot\text{OH}$ is one of the main radicals involved in diseases and metabolism, while $\cdot\text{CH}_3$ may be released through different paths derived from reactions wherein $\cdot\text{OH}$ is involved [12]. In order to gain insight into the molecular orbital reactivity, this study was carried out chiefly through energy and charge decomposition analysis. Afterwards, in order to find out if there is any additional factor capable of affecting the reaction pathways, non-covalent interactions were analyzed by the reduced density gradient (RDG) method [13], derived from AIM analysis [14], which results reliable for both simple and complex systems containing either a few, or many atoms [15]. Thus, in order to rationalize the resulting theoretical models, the usual magnitude of the hyperfine coupling constants obtained from spin-trapping experiments were taken from previous reports (or spin-trap databases) and compared with our theoretical results.

2. Methodologies

2.1. Theoretical procedures

Unless indicated otherwise, the standard procedures were as follows: the initial structural models for reactants and products were built with Spartan 10 [16]. Minimum energy conformers were located by MMFF and optimized later with semiempirical (AM1)

methods. All following calculations were performed with Gaussian 09 [16]. Resultants geometries were re-optimized by AM1 at a full convergence criterion (very tight). The first guesstimate to the transition state (TS) was performed with QST2 [17] at AM1 level, and the intrinsic reaction coordinate (IRC) was estimated later at the same theory level. Afterwards, starting from the IRC results the resultant structures for reactants and products were taken (also optimized as described above) and used as initial guess for a QST3 calculation at AM1 level again (the initial guess for the TS structure corresponded to that of the QST2 calculation) and the IRC was calculated. Each TS structure was confirmed and characterized by a single negative (imaginary) frequency. The frequencies for all stationary points are available as supplementary information (SI)†.

Afterwards, starting from the QST3 calculation results (at AM1 level), the structures for reactants and products were taken and subsequently used as guess structures for high theory-level calculations. Final TS and IRC calculations were performed with QST2 (or QST3) at (U)B3LYP/6-31G(d) level [18,19], and the reactants (and products) were re-optimized at the referred level. Additionally, solvation effects were included in calculations for TS, IRC, reactants and products by the continuous surface charge polarizable continuum model [20]. The optimized geometries resulted in complete agreement with the available X-ray crystallography data for the bond lengths N1=C2, N1-O6 (as spin-trap), N1-C2 and N1-O6 (as spin-adduct) [21–23]. The optimized geometries are available as supplementary information (SI)†. Single point calculations for spin-adducts were performed at (U)B3LYP/6-31G(d) [24] level together with the aforementioned solvation model previously described as a proper model to estimate the hyperfine interactions [25].

Mulliken population analysis (MPA), energy decomposition analysis (EDA) [26,27], charge decomposition analysis (CDA) [28,29] (as well as its extended version ECDA) [30,31], orbital interaction diagrams, and partial/total density of states plots were performed with AOMix [32]. Total and partial density of states plots are scaled by 1/2. Fragments for population analysis were partitioned in terms of the Dewar-Chatt-Duncanson model. Atomic charges and spin densities were calculated at (U)B3LYP/6-31G(d) (PCM) level under MPA and NPA [33] (implemented by NBO5.G [34]) partition models. Analysis of the wavefunction such as RDG [13], AIM [14] and CT analysis based on the Le Bahers' method [35] were performed with Multiwfn [36]. Isosurfaces were built with Avogadro [37] or VMD [38], and traced with POV-Ray [39]. Details about acronyms and abbreviations are summarized in supplementary information (SI)†.

3. Results

3.1. REACTION 1: DMPO + $\cdot\text{OH} \rightarrow \cdot\text{DMPO-OH}$

3.1.1. Intrinsic reaction coordinate

The reaction pathway for the entrapment reaction between the hydroxyl radical and DMPO (Fig. 2) begins by reducing the distance between O20 and C2 in parallel to the variation of the dihedral angle formed by C2-C3-C4-H10 in such way that this angle varies drastically from 143.05° to 97.83° what makes that C2 gets closer to O20 shortening its distance from 3.5 Å to 2.2 Å. Subsequently, the distance between H21 and O6 is slightly increased until DMPO reaches a flat conformation with an angle close to zero for the dihedral C2-C3-C4-C5. After that, the distance H21-O6 is further increased (~0.75 Å), and the H15 (partially) gets out of the ring plane, thus reaching the transition state. In the downhill of the reaction pathway, the distance O20-C2 is shortened until 1.4 Å whereas the C2-N1 bond is lengthened in 0.11 Å, thus leading to the formation of the single bond O20-C2. In parallel to the above, to the extent to which C2 gets closer to O20 (mainly through the

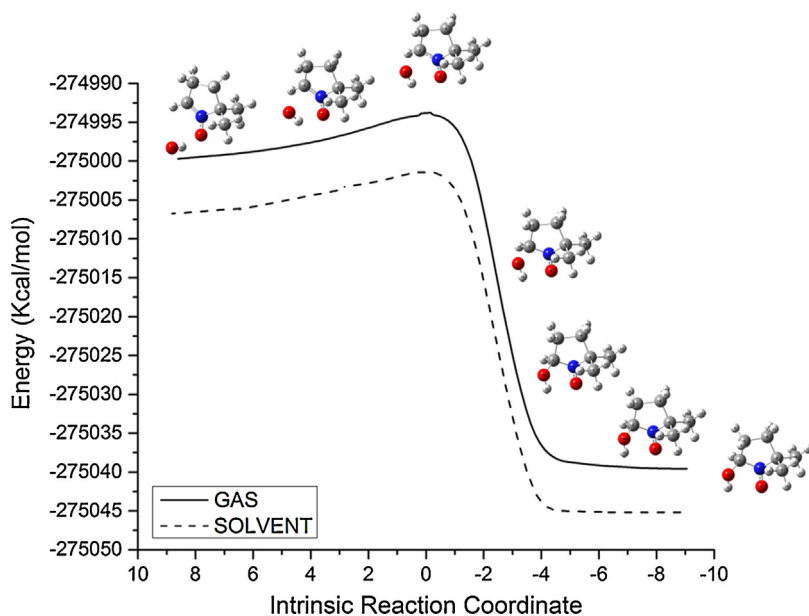


Fig. 2. Intrinsic reaction coordinate for the entrapment reaction between the hydroxyl radical and the spin-trap DMPO. Main geometrical changes along the IRC were included.

change in the dihedral C2–C3–C4–H10 from 97.83° to 106.78° , H15 moves away from C2 converging in an angle for H15–C2–C20 closer to a sp^3 -like form (109.75°). Thus, after forming the bond, the spin-adduct reaches its minimum energy along the path predominantly by the change in the dihedrals C2–C3–C4–H10 (from 106.78° to 87.15°) and N1–C2–O20–H21 ($\sim 8^\circ$) thus reaching the bottom of the intrinsic reaction coordinate for the formation of the spin-adduct ${}^{\bullet}\text{DMPO-OH}$. Energies parameters are summarized in Table 1. Additionally, a 3D animation containing main distance variations along the IRC (see supplementary information).

3.1.2. Molecular orbital interaction and energy decomposition analysis

In order to assess how the molecular orbitals of each fragment interact to give effect to the reaction pathway, molecular orbital interaction diagrams were constructed. For reactants, at first sight, there is no evidence of significant interactions between the hydroxyl radical and DMPO in the nearby of HOMO–LUMO gap (Fig. 3A). In fact, H-0, H-1 and H-2 show a small interaction degree which ranges from 1% to 4%, and therefore, with a low involvement at the beginning of the reaction. However, at an innermost zone a greater interaction between DMPO and ${}^{\bullet}\text{OH}$ begins to be observed (Fig. 3B), where H-1 (α and β) from ${}^{\bullet}\text{OH}$ interacts with almost all orbitals between H-6 and H-11 from DMPO, leading to a series of interacting orbitals (from H-7 to H-12) with a greater contribution of both fragments, and possibly with a bigger involvement at the beginning of the reaction. From the molecular orbital diagram, it is difficult however to accurately identify which are the main orbitals involved in the reaction because there are several medium-range interactions. The latter is in agreement with

the various geometric perturbations previously described for the beginning of the reaction, which would be ruled by the multiple interactions at the innermost zone, and not by a few ones at the HOMO–LUMO gap.

Continuing along the reaction pathway and, due to the multiple interactions present, it seems meaningless to analyze the intermediate states by which, the next state to be examined is the transition state (TS). Thus, having attained the TS, the scenario changes drastically and the orbitals involved in the binding interaction begin to be more evidently seen. As shown in Fig. 4, both $[\text{HOMO}]^\pm$ and $[\text{LUMO}]^\pm$ from DMPO interact with $[\text{LUMO}(\beta)]^\pm$ and $[\text{HOMO}(\beta)]^\pm$ from ${}^{\bullet}\text{OH}$ giving rise to a series of β transition orbitals such as $[\text{H-1}(\beta)]^\pm$, $[\text{H-0}(\beta)]^\pm$, $[\text{LUMO}+0(\beta)]^\pm$ and $[\text{L}+1(\beta)]^\pm$, of which, $[\text{H-1}(\beta)]^\pm$ and $[\text{H-0}(\beta)]^\pm$ display a bonding character evidenced both by, the density of the overlapped populations ($\text{OPDOS} > 0$), as well as by the form of the isosurfaces of such orbitals, clearly connecting C2 with O20 along the y axis (see Fig. 5A). Likewise, the interaction between $[\text{H-1}(\alpha)]^\pm$ (from ${}^{\bullet}\text{OH}$) with $[\text{HOMO}]^\pm$ (from DMPO) leads to the formation of a series of orbitals, of which, the most relevant ones are $[\text{HOMO}-0(\alpha)]^\pm$ and $[\text{H-3}(\alpha)]^\pm$. The first one, with clear antibonding character ($\text{OPDOS} < 0$), is feasible to be predicted as the host orbital for the unpaired electron, whereas the second one, presumably involved in the formation of the bond, as is evidenced by the bonding character ($\text{OPDOS} > 0$) of the orbital (see Fig. 5A).

To the extent to which the transition orbitals evolve toward their “final state” (as product), the MO diagram discloses (Fig. 6), as expected, that for the spin-adduct ${}^{\bullet}\text{DMPO-OH}$, the unpaired electron would reside in the antibonding orbital $\text{HOMO}-0(\alpha)$. However, the nature of this orbital arises as a consequence of

Table 1

Theoretical energy parameters resultant from trapping reactions.^a

Reaction	$-E_{\text{Reactants}}$ (a.u.)	ΔE^\ddagger (kcal mol $^{-1}$)	$-\Delta G$ (kcal mol $^{-1}$)	$-\Delta G^\ddagger$ (kcal mol $^{-1}$)
$\text{DMPO} + {}^{\bullet}\text{OH} \rightarrow {}^{\bullet}\text{DMPO-OH}$	441.000 (440.917)	0.602 (0.710)	46.643 (47.685)	ND (46.635) ^b
$\text{DMPO} + {}^{\bullet}\text{CH}_3 \rightarrow {}^{\bullet}\text{DMPO-CH}_3$	405.028 (405.020)	3.177 (4.202)	45.900 (46.949)	ND (33.468) ^b

^a Theoretical values were obtained at a UB3LYP/6-31G(d) theory level under solvation considerations. In round brackets are indicated the corresponding values under vacuum conditions. Energy units were chosen in this way for easier comparison between reactions.

^b Values were taken from the supplementary material of Ref. [10] (calculated at the same theory level) and the units were adapted according to $0.9806 \text{ a.u.} = 627.5095 \text{ kcal mol}^{-1}$. $\Delta E^\ddagger = E_{\text{TS}} - E_{\text{Reactants}}$. $\Delta G = E_{\text{Adduct}} - E_{\text{Reactants}}$. ND = not available data.

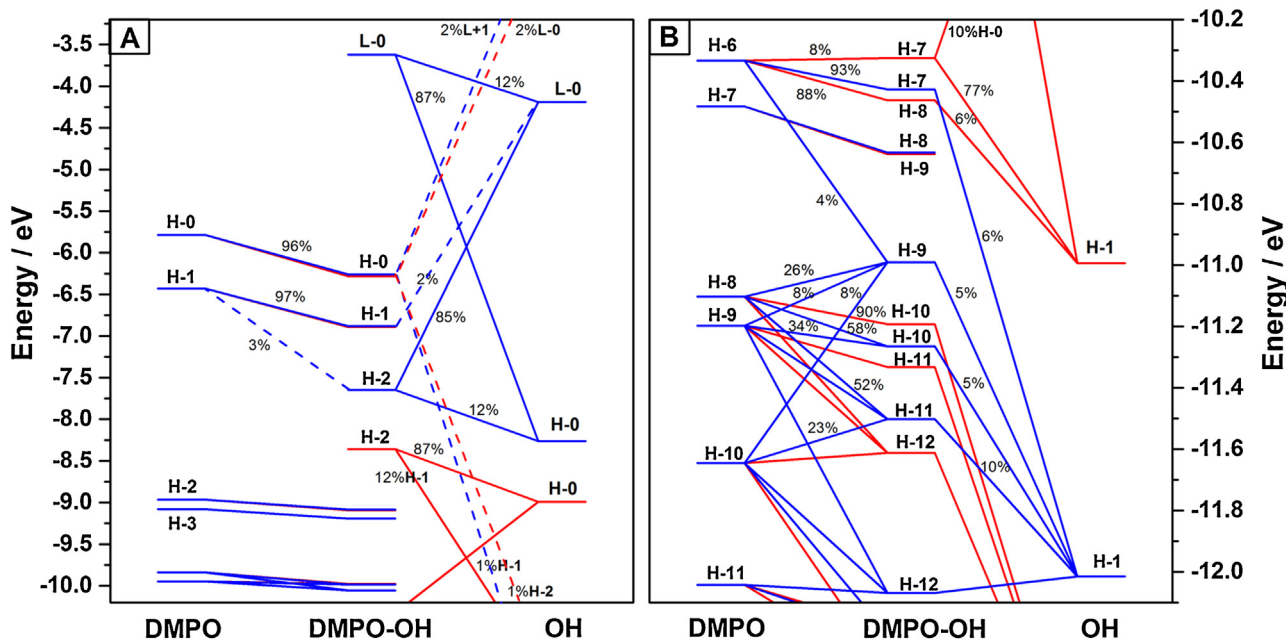


Fig. 3. Orbital interaction diagram for the reactants of the entrapment reaction between the hydroxyl radical and the spin-trap DMPO. Spin orbitals are shown as red (α) and blue (β) lines, respectively. All contributions were included. Connecting lines for contributions lower than 4% are shown as dotted lines, while those upon this threshold as continuous lines, respectively. (For interpretation of the references to color in this text, the reader is referred to the web version of the article.)

the combination HOMO–LUMO from DMPO, which (energetically speaking) are “barely” affected by the presence of $\cdot\text{OH}$ along the reaction path; in fact, most energy levels of the orbitals of DMPO and $\cdot\text{OH}$ are only slightly perturbed to the extent they come together. Notwithstanding the aforementioned, the role of $\cdot\text{OH}$ in the reaction is relevant since it allows the interaction between the HOMO–LUMO orbitals of DMPO, null at the beginning of the reaction, but evident in the TS (chiefly through H-0(α) of $\cdot\text{OH}$), as well as in the spin-adduct; for the latter, however, it is given by the H-1(α) of $\cdot\text{OH}$. In this manner, the contributions of LUMO (from DMPO) to HOMO-0(α)_{DMPO-OH} are considerably increased, while

those of HOMO (from DMPO) are slightly decreased, until both reach the product state (spin-adduct). Thus, the interaction with $\cdot\text{OH}$ allows the combination of the HOMO–LUMO orbitals of DMPO, which leads to the formation of HOMO-0(α) and that ultimately will host the unpaired electron.

3.1.3. Reduced density gradient analysis

As noted above, the beginning of the entrapment reaction between DMPO and $\cdot\text{OH}$ is mainly directed by a multiple interaction phenomenon between reactants. Consequently, this outcome suggests that, at least, the beginning of the reaction is governed by the

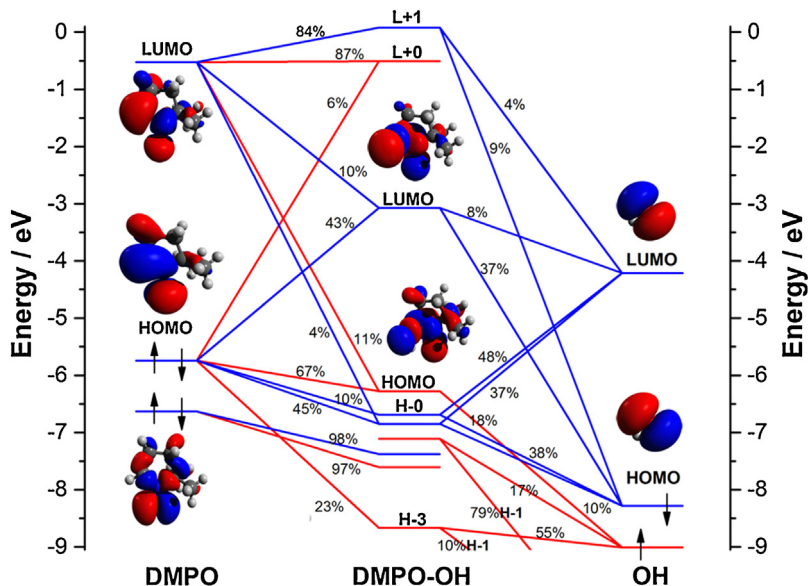


Fig. 4. Orbital interaction diagram for the transition state $[\text{DMPO} \cdots \cdot\text{OH}]^\#$. Spin orbitals are shown as red (α) and blue (β) lines, respectively. Connecting lines for contributions higher than 4% are included in the MO diagram. Selected MO isosurfaces were included to an isovalue of ± 0.02 . (For interpretation of the references to color in this text, the reader is referred to the web version of the article.)

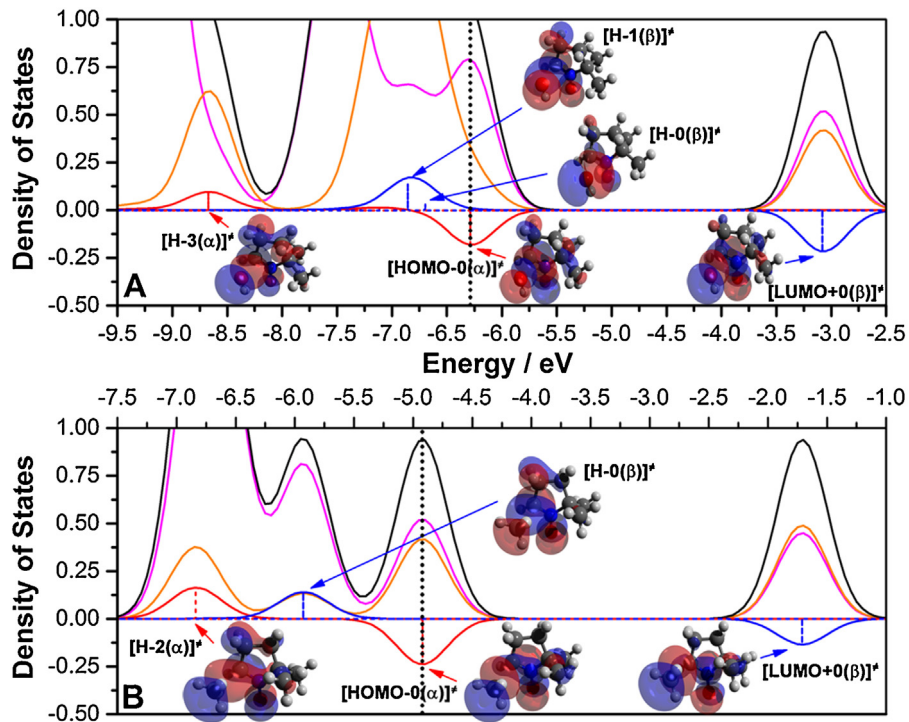


Fig. 5. Density of states plot for the transition states (A) $\bullet^*[\text{DMPO}\cdots\text{OH}]^\pm$ and (B) $\bullet^*[\text{DMPO}\cdots\text{CH}_3]^\pm$. Continuous lines correspond to the total (black), partial-DMPO (purple), partial-radical (orange), α -overlap (red) and β -overlap (blue) density of states. All PDOS, TDOS and OPDOS values in continuous plots are scaled by 1/2. Dotted vertical lines indicate the position of highest (single) occupied molecular orbital. Selected MO isosurfaces were included to an isovalue of ± 0.02 .

sum of such interactions, and therefore, it is feasible to be expressed as a weak interaction component. Thus, in order to assess how do these interactions could modulate the beginning of the reaction, a weak interactions analysis was performed according to the reduced density gradient (RDG) method based on the AIM theory [13].

RDG analysis for the reactants reveals three types of weak interactions (see Fig. 7A): a steric clash in the middle of the pentagonal ring (red isosurface), three interactions in the Van der Waals (VdW) region (brown-green light isosurfaces), and a strong H-bond between H21 and O6 (dark blue isosurface). The

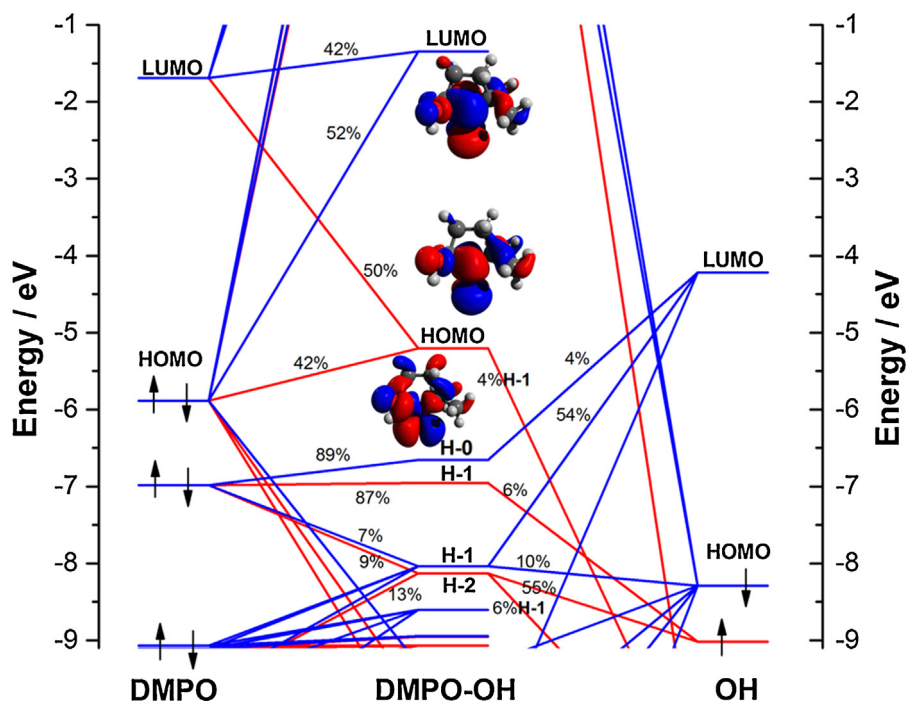


Fig. 6. Orbital interaction diagram for the spin-adduct $\bullet^*[\text{DMPO}\cdots\text{OH}]^\pm$. Spin orbitals are shown as red (α) and blue (β) lines, respectively. Connecting lines for contributions higher than 4% are included in the MO diagram. Selected MO isosurfaces were included to an isovalue of ± 0.02 . (For interpretation of the references to color in this text, the reader is referred to the web version of the article.)

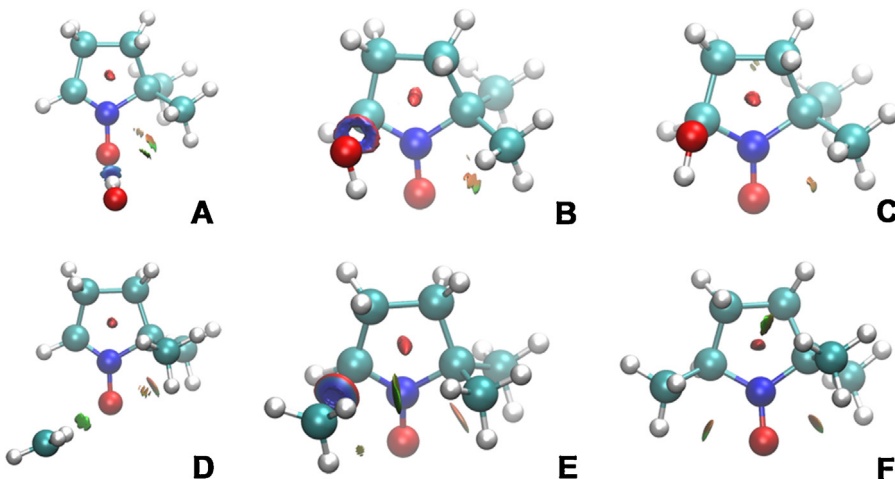


Fig. 7. Isosurfaces for weak interactions along the trapping reaction. At the top, isosurfaces for the trapping of $\cdot\text{OH}$ by DMPO for (A) reactants, (B) transition state and (C) product. At the bottom, those corresponding to the trapping of $\cdot\text{CH}_3$ for the states of (D) reactants, (E) transition state and (F) product.

latter is particularly interesting since as was described in the IRC section, at the beginning of the reaction, the distance $\text{H}21 \cdots \text{O}6$ remained practically constant to the extent that $\text{O}20$ gets closer to $\text{C}2$, all of which suggests that the H-bond governs the initial state of the reactants until the orbital interaction strengths surpass the first ones, causing that $\text{H}21$ moves away from $\text{O}6$, thus attaining the TS. Moreover, the search for critical points based on AIM topology analysis reveals a $(3,-1)$ bond critical point (BCP) between $\text{O}6$ and $\text{H}21$ (indeed corresponding to the hydrogen bond) whose energy is about $E_{\text{HB}}(\text{O}6-\text{H}21) = -45.90 \text{ kJ/mol}$ (according to relationship $E_{\text{HB}} = V_{(\text{BCP})}/2$) [40], which confirms the significant role of this interaction, because it clearly exceeds the typical H-bond energies (-15 to -30 kJ/mol), and ranks it between the boundaries of a strong H-bond and the covalent limit (-40 to -50 kJ/mol) [41].

On the other hand, at the TS, the steric and VdW interaction regions are conserved, the $\text{H}\text{-bond}_{(\text{O}6 \cdots \text{H}21)}$ ceases to exist, and a strong interaction emerges between $\text{C}2$ and $\text{O}20$ (see Fig. 7B). Interestingly, the latter exhibits an annular shape constituted by an internal attractive zone (blue dark), and a repulsive area (strong red) which covers a part of the boundary isosurface. Curiously, a “hole” in the middle of the isosurface reveals an exclusion zone, free from weak interactions which is crossed by the y axis (previously found as the reaction axis) and containing a BCP between $\text{C}2$ and $\text{O}20$. This particular shape could suggest that the reacting species are in the point at which the orbitals are effectively overlapped to conduct the formation of the bond between $\text{O}20-\text{C}2$, and therefore, can be seen as the response of the proper rearrangement of the orbitals involved in the formation of the bond, or maybe, as a fixing factor of the reacting species in favor of an adequate orbital interaction.

To conclude, after the formation of the bond, and having reached the minimum along the IRC, RDG analysis on the spin-adduct $\cdot\text{DMPO-OH}$ (product) exhibits a steric region and two VdW regions as shown in Fig. 7C. Beside the above, additional BCP or weakly interacting regions were not found.

3.1.4. Spin density and ECDA for charge transfer

At the reactant state, the spin density is mainly focused on the hydroxyl radical (isosurface in Fig. 8A) and particularly on $\text{O}20$ (Fig. 9A). However, spin density plots on the plane conformed by $\text{N}1-\text{C}2-\text{O}6$ predicts a small spin polarization on the nucleus $\text{O}6$ and $\text{C}2$ (Fig. 8A). Afterwards, insofar that the reacting species reach the TS, the spin density in DMPO is increased

strongly on $\text{O}6(\alpha)$ and partially on the nuclei $\text{N}1(\alpha)$ and $\text{C}2(\beta)$ (Fig. 8B). The latter one, with a (negative) peak which points toward the corresponding maximum in $\text{O}20(\alpha)$ through the y coordinate (Figs. 8B and 9A,B), would allow us to anticipate a charge transfer phenomenon between the hydroxyl radical and DMPO.

In fact, extended charge decomposition analysis (ECDA) confirms the polarization of the DMPO's alpha orbitals ($[\text{PL(DMPO)}]_\alpha \neq -[\text{PL}(\cdot\text{OH})]_\alpha \neq = 0.0561$), and the electron donation from $\cdot\text{OH}$ to DMPO ($[\text{CT(DMPO} \rightarrow \cdot\text{OH})]_\alpha \neq -[\text{CT}(\cdot\text{OH} \rightarrow \text{DMPO})]_\alpha \neq = -0.0844$) mainly provided by $[\text{H-0}(\alpha)] \neq (0.046$ according to the Dapprich scheme [28]) and to a lesser extent by $[\text{H-1}(\alpha)] \neq$, $[\text{H-3}(\alpha)] \neq$ and others. Secondly, the beta electrons are also transferred, but this time, from DMPO to $\cdot\text{OH}$ ($[\text{CT(DMPO} \rightarrow \cdot\text{OH})]_\beta \neq -[\text{CT}(\cdot\text{OH} \rightarrow \text{DMPO})]_\beta \neq = 0.3843$) and accompanied by a strong polarization term in $\cdot\text{OH}$ ($[\text{PL(DMPO)}]_\beta - [\text{PL}(\cdot\text{OH})]_\beta = -0.4215$). Thus, the net electron transfer mainly comes from DMPO to be transferred to $\cdot\text{OH}$ in the TS stage ($[\text{CT(DMPO} \rightarrow \cdot\text{OH})]_{(\alpha+\beta)} \neq -[\text{CT}(\cdot\text{OH} \rightarrow \text{DMPO})]_{(\alpha+\beta)} \neq = 0.2998$). Indeed, in agreement with the simplest chemical sense of electronegativity in which the electron transfer goes toward the most electronegative atom, being in this occasion, the oxygen's nucleus of the $\cdot\text{OH}$.

To conclude, having reached the minimum along the reaction coordinate, the spin density on the fragment $\text{O}20-\text{H}21$ (previously $\cdot\text{OH}$ radical but now bound to the spin-trap) is clearly diminished just leaving a small remnant of the population on $\text{O}20$ (Fig. 9A), but increasing partially that of $\text{N}1$, and considerably that of $\text{O}6$ (Fig. 9C). From another angle, to the extent that the TS turns into the product, the spin density along the bond $\text{C}2-\text{H}15$ remains practically unperturbed and chiefly localized at both nuclei (Fig. 9B), suggesting that there is no significant changes in the spin density distribution. However, the latter result would lack meaning mainly by the observed differences between the experimental and calculated hyperfine coupling constants (see Table 2), most

Table 2

Hyperfine coupling constants for the adducts $\cdot\text{DMPO-OH}$ and $\cdot\text{DMPO-CH}_3$.

Spin-adduct	$a_{\text{N}1}/\text{Gauss}$	$a_{\text{H}15}/\text{Gauss}$
$\cdot\text{DMPO-OH}$	11.82 (15.20)	5.73 (14.60)
$\cdot\text{DMPO-CH}_3$	12.95 (15.41)	24.27 (23.05)

Theoretical and experimental (in round brackets) HFCCs were obtained at a UB3LYP/6-31G(d) theory level under solvation considerations. Experimental HFCCs were taken from Ref. [12].

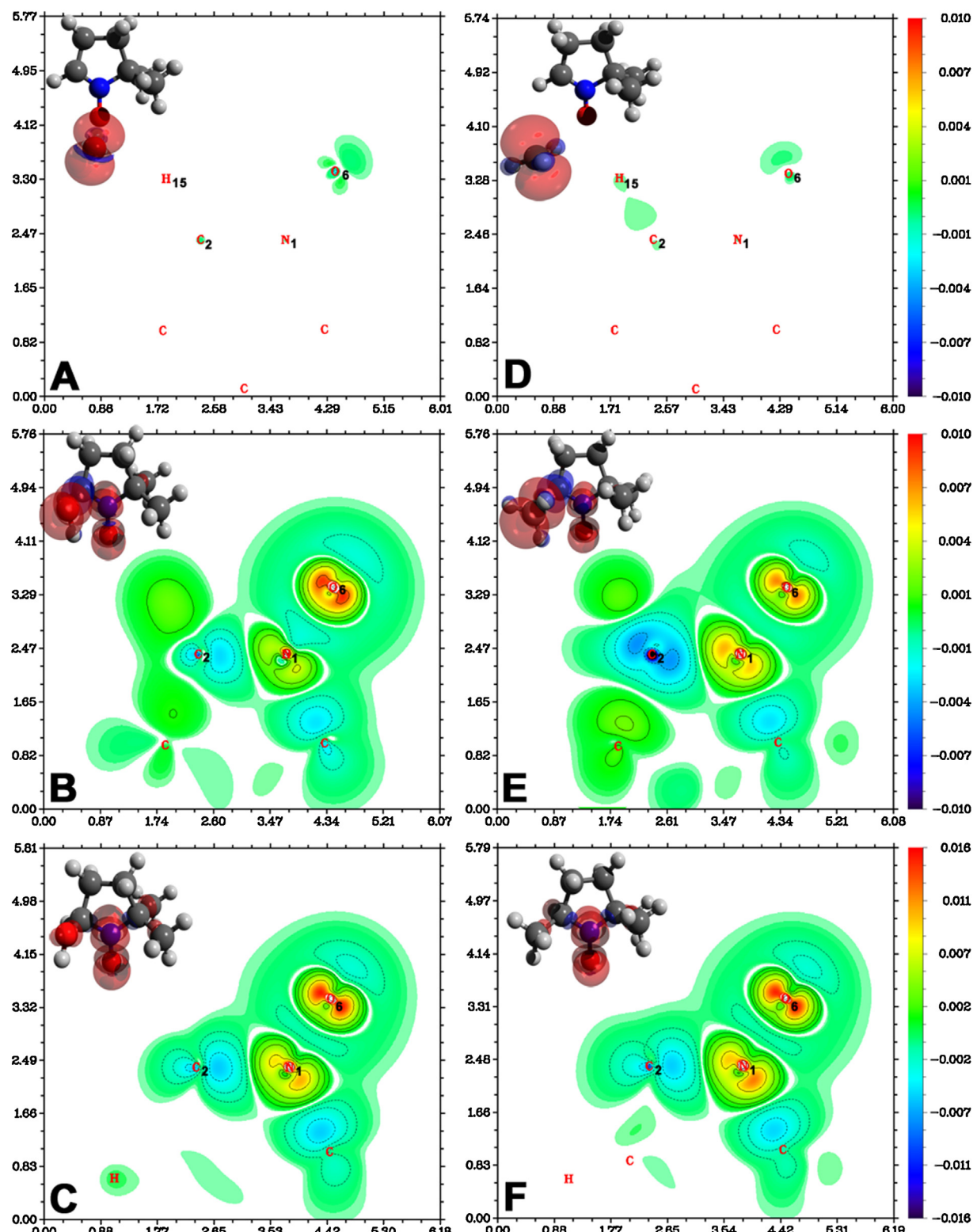


Fig. 8. Spin density plots along the plane conformed by N₁–C₂–O₆ for (A and D) reactants, (B and E) TS and (C and D) product for the trapping of OH (left column) and CH₃ (right column) by DMPO. Colors were filled according to the attached legend (right side) in a.u. The background color was removed for easy viewing. Plane coordinates in Å units. In the top left corner are included the isosurfaces (α = red; β = blue) for the spin density (isovalue = 0.002). (For interpretation of the references to color in this text, the reader is referred to the web version of the article.)

likely due to an improper final geometry for the spin-adduct.

Thus, the calculated hyperfine coupling constant would correspond to a state closest to the transition structure instead of one

in neighborhoods close to the spin-adduct, which is why the calculated HFCCs for N1 and H15 are underestimated regarding the experimental values. Thus, despite the fact that the deviation in the prediction of the HFCCs occurs mainly on H15, the prediction

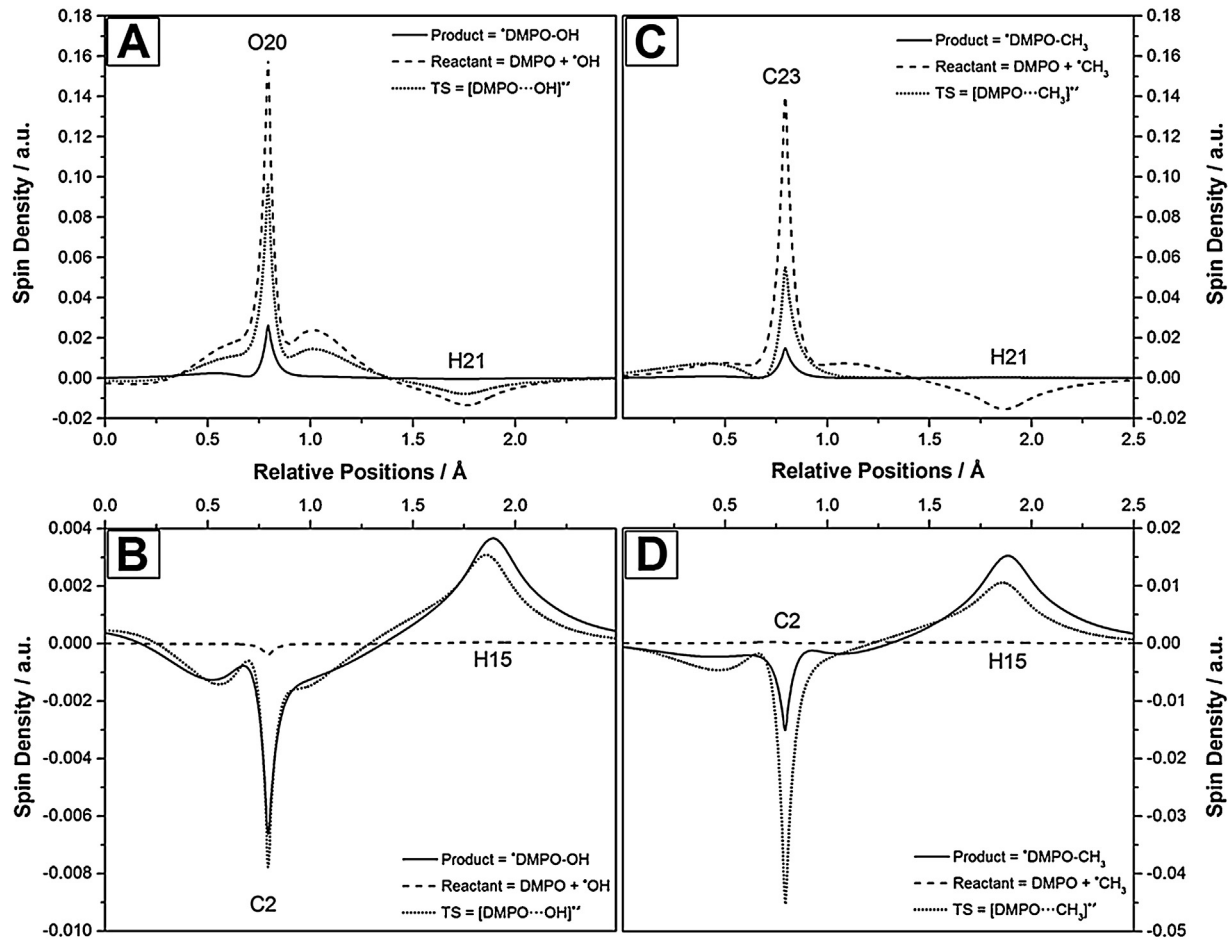


Fig. 9. Spin density variations along (A) O20–H21 and (B) C2–H15 for the trapping of $\cdot\text{OH}$, (C) C23–H21 and (D) C2–H15 for the trapping of $\cdot\text{CH}_3$. Dashed, dotted and continuous lines correspond to reactants, TS and product, respectively.

for N1 is still good enough to think in this model as base for further improvements, but always taking into account the evident deficiency in the partition model.

3.2. REACTION 2: $\text{DMPO} + \cdot\text{CH}_3 \rightarrow \cdot\text{DMPO-CH}_3$

3.2.1. Intrinsic reaction coordinate

Contrasting the previous reaction, the beginning of the reaction between the methyl radical and DMPO takes place through a more direct route and without major perturbations regarding the initial geometry (Fig. 10). Namely, most angles and bond lengths of each reactant are conserved, with the logical exception of the distance C23···C2 which is shortened in 0.98 Å through a pivotal movement (H20 is the pivot point), possibly involving the simultaneous displacement of C23, H21 and H22, which would preserve both, the angles and the bond lengths of the methyl radical. The latter would, in turn, lead to approaching of the reactants, but without losing the initial semi-flat geometry of the methyl radical (A → B in Fig. 10). Subsequently, the distance C23···C2 is shortened over again, but now leaving fixed H20, H21 and H22, which renders the methyl radical acquires an angular geometry, while C2 (from DMPO) moves away from N1 by 0.05 Å (bond length N1–C2 = 1.34 Å), thus reaching the TS (B → C in Fig. 10).

In a straightforward way, the distance C23···C2 continues being shortened by the approaching of the methyl radical and the lengthening of the bond C2–N1, which makes the latter adopt a bond length of 1.47 Å (now as a single bond) (C → D in Fig. 10) and later, a few steps

forward, achieve the binding between C23–C2 (D → E in Fig. 10). Finally, having accomplished the trapping of the methyl radical, the spin-adduct would reach its minimum energy mainly by rotating the methyl group (previously methyl radical) accompanied by a small contraction of the bond N1–2C (~0.01 Å) and slight rearrangements of the spin-adduct, thus reaching the product state along the IRC (E → G in Fig. 10). Energies parameters are summarized in Table 1. Additionally, a 3D animation containing main distance variations along the IRC (see supplementary information).

3.2.2. Molecular orbital interaction and energy decomposition analysis

As is shown in Fig. 11, the MO interacting diagram for the reactants reveals that the reaction begins immediately with a significant MO interaction and mainly given by a HOMO–HOMO interaction between both reactants. As a result of this interaction, three orbitals are formed: HOMO-2(α), HOMO-1(β) and HOMO-0(α), of which, HOMO-2(α) is chiefly constituted by $\cdot\text{CH}_3$ (~88%) and particularly by C23, which contributes with a 49%py and 39%px. In turn, DMPO (~12%) does it by means of O6 through 7%pz. On the other hand, HOMO-1(β) does not exhibit interaction whatsoever with $\cdot\text{CH}_3$, and consequently all contributions to the orbital are given by the DMPO's HOMO through O6 (50%pz), C2 (28%pz) and N1 (3%pz). Just above, the orbital HOMO-0(α) displays a greater contribution by DMPO (~88%) mainly given by O6 (44%pz) and C2 (25%pz), while $\cdot\text{CH}_3$ (~12%) does it through C23 by 6%py and 3% (each pz and px).

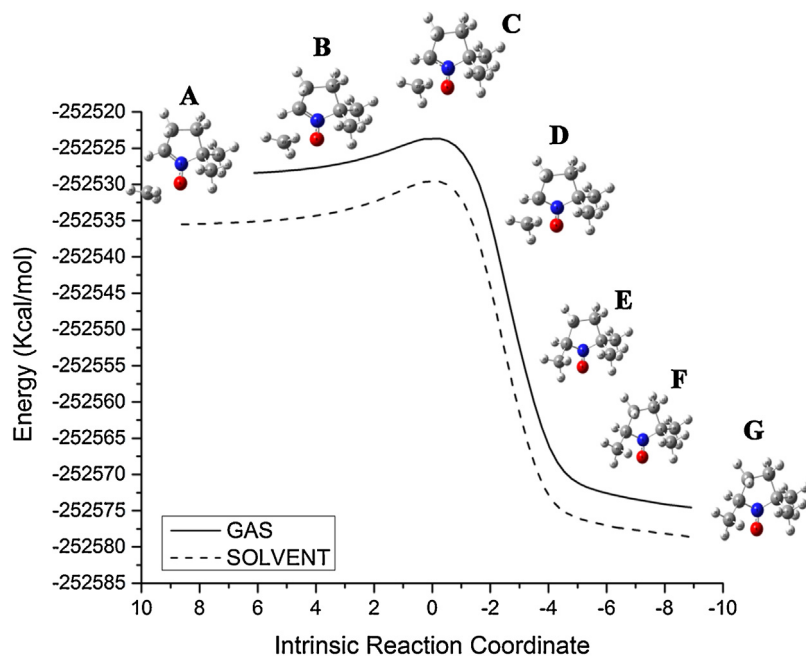


Fig. 10. Intrinsic reaction coordinate for the entrapment reaction between the methyl radical and the spin-trap DMPO. Main geometrical changes along the IRC were included.

However, when reaching the transition state, the scenario changes dramatically. As is shown in Fig. 12 (and comparing it with Fig. 11), a small narrowing in HOMO–LUMO gap can be seen in both fragments. Consequently, due to the proper orbital alignment (along the y axis), both $\text{HOMO}(\alpha,\beta)_{\text{DMPO}} \neq$ as $\text{LUMO}(\alpha,\beta)_{\text{DMPO}} \neq$ are combined with $\text{HOMO}(\alpha)_{\text{CH}_3} \neq$ and $\text{LUMO}(\beta)_{\text{CH}_3} \neq$ which converges into the formation of six relevant transition orbitals, some of which ($[\text{LUMO-0}(\beta)] \neq$ and $[\text{H-0}(\beta)] \neq$) also allow the interaction between the own frontier orbitals of DMPO, $\text{HOMO}(\alpha,\beta)_{\text{DMPO}} \neq$ and $\text{LUMO}(\alpha,\beta)_{\text{DMPO}} \neq$ (Fig. 12).

Upon analyzing the contributions of the transition orbitals, p_i orbitals emerge over again as the main involved in the interaction. For instance, the major contributions to $[\text{HOMO}(\alpha)] \neq$ come from py orbitals ($C23 = 43\%$; $O6 = 24\%$; $N1 = 17\%$). Thus, just like the TS $^{\bullet}[\text{DMPO}\cdots\text{OH}]$, the antibonding orbital $[\text{HOMO-0}(\alpha)] \neq$ ($\text{OPDOS} < 0$, see Fig. 5B) is the responsible for allocating the unpaired electron. Right below $[\text{HOMO-0}(\alpha)] \neq$, the orbital $[\text{H-0}(\beta)] \neq$ is clearly revealed as one of the orbitals involved in binding both fragments ($\text{OPDOS} > 0$, Fig. 5B), and whose contributions come mainly from $C2(40\%)$ and to a lesser extent from $O6(28\%)$ and $C23(13\%)$.

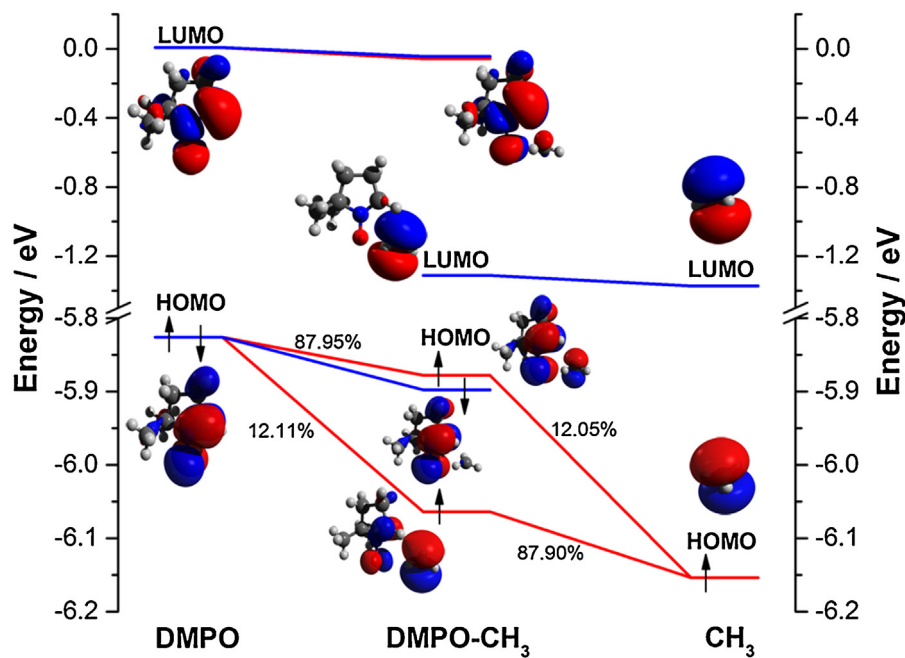


Fig. 11. Orbital interaction diagram for the reactants of the entrapment reaction between the methyl radical and the spin-trap DMPO. Spin orbitals are shown as red (α) and blue (β) lines, respectively. Connecting lines for contributions higher than 4% are included in the MO diagram. Selected MO isosurfaces were included to an isovalue of ± 0.02 . (For interpretation of the references to color in this text, the reader is referred to the web version of the article.)

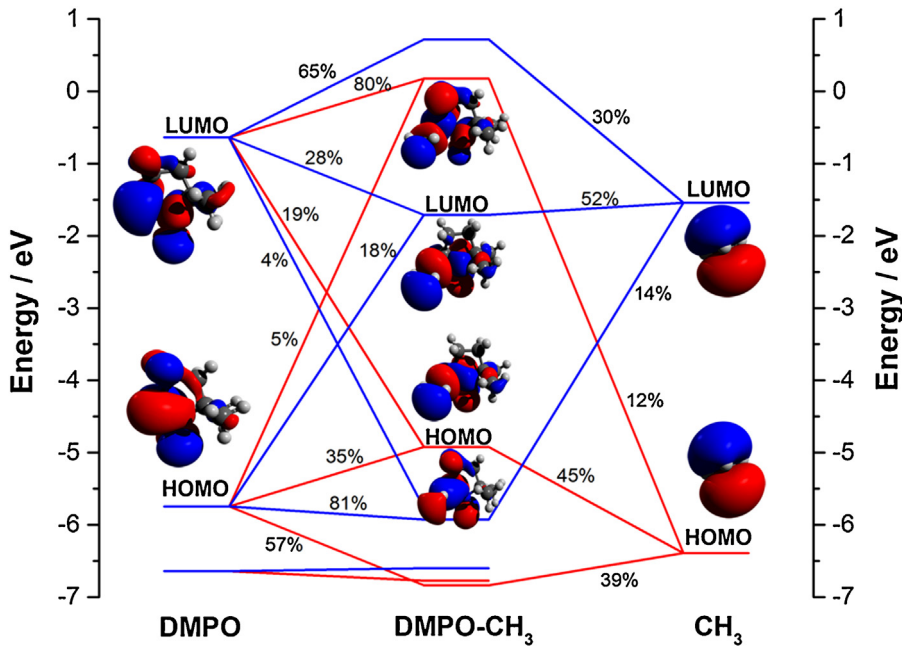


Fig. 12. Orbital interaction diagram for the transition state $\cdot[DMPO \cdot \cdot CH_3]^{\ddagger}$. Spin orbitals are shown as red (α) and blue (β) lines, respectively. Connecting lines for contributions higher than 4% are included in the MO diagram. Selected MO isosurfaces were included to an isovalue of ± 0.02 . (For interpretation of the references to color in this text, the reader is referred to the web version of the article.)

Likewise, the bonding orbital $[H-2(\alpha)]^{\ddagger}$ provides the α counterpart to the formation of the bond ($OPDOS > 0$, Fig. 5B), and as might be expected, the greatest contributions are now given by C23 (37%) and to a lesser extent by C2(21%) and O6(18%), and once more, all contributions mentioned above for $[H-0(\beta)]^{\ddagger}$ and $[H-2(\alpha)]^{\ddagger}$ take place through *py* orbitals along the *y* axis (matters concerning the charge transfer phenomenon will be discussed later). Thus, the transition structure is achieved by the rearrangement of the electron populations on *py* orbitals in order to accomplish the proper orbital alignment and success in binding interactions, requirements which are achieved to the extent that the $\cdot CH_3$ gets closer to DMPO, thus allowing to disclose the *y* coordinate as the reaction axis.

Afterwards, going down along the IRC, the MO diagram for the spin-adduct (Fig. 13) indicates that, to the extent to which the TS turns into the product, the orbitals of DMPO are split into their α and β components to such a degree that allows the formation of new spin restrained connections that completely change the orbital composition of the adduct. Accordingly, for instance, while the orbital $LUMO-0(\beta)_{DMPO-CH_3}$ arises from the combination between $L+0(\beta)_{DMPO}$ and $L+1(\beta)_{DMPO}$, the $HOMO-0(\alpha)_{DMPO-CH_3}$ is constituted mainly by the combination $H-0(\alpha)_{DMPO}$ and $H-2(\alpha)_{DMPO}$, thereby converging in that, neither $HOMO-0(\alpha)_{DMPO-CH_3}$ nor $LUMO-0(\beta)_{DMPO-CH_3}$ establish a significant connection with the unoccupied or occupied orbitals of each fragment, respectively. Thus, the final scheme of the MO interactions differs considerably from that described for the adduct $\cdot DMPO-OH$, what will ultimately have the greatest impact on HFCCs as will be discussed further on later sections.

3.2.3. Reduced density gradient analysis

As was shown, unlike the reaction with the hydroxyl radical, the reaction between the methyl radical and DMPO is ruled from the beginning by significant MO interactions. However, some differences in the framework of weak interactions can be established. Thus, RDG analysis on the reactants (Fig. 7D) reveals a steric region at the inner zone of the DMPO ring (red isosurface), two intermediate repulsion regions (brown light) with small contributions in the VdW zone (green), and a pure VdW region between H2O

and O6 (green isosurface). Similar to the reaction with $\cdot OH$, AIM analysis discloses a BCP between H2O and O6, wherein, by treating it as a weak H-bond, its energy is $E_{HB(H2O-O6)} = -12.92$ kJ/mol, lower than the H-bond between $\cdot OH$ and DMPO previously described. However, this is not a H-bond actually, and must be seen only as an approach to illustrate the decrease in the interaction energy. Notwithstanding, this interaction should be, undoubtedly, responsible for the pivotal movement of $\cdot CH_3$ in the first steps of the reaction to give way then to increased MO interactions as was previously described.

Subsequently, at the TS, weak interactions for $\cdot[DMPO \cdot \cdot CH_3]^{\ddagger}$ (Fig. 7E) were comparable at all to those described for $\cdot[DMPO \cdot \cdot OH]^{\ddagger}$. Thus, the steric region (red isosurface) and the strong attraction zone between C2 and C23 are comparable to that described between C2 · · O20 for the case of $\cdot[DMPO \cdot \cdot OH]^{\ddagger}$. However, the latter, unlike that of $\cdot[DMPO \cdot \cdot OH]^{\ddagger}$, the isosurface is fully filled with a strong blue color, thus suggesting that at the TS, the reactants have to get even closer for carrying out the trapping successfully, in fact, this reading is in complete agreement with the above described pathway, at which, the main geometrical changes on DMPO occur in the vicinity of the TS toward the formation of the product through the lengthening of the bond C2–N1 in conjunction with the approaching of $\cdot CH_3$. Furthermore, as expected, a BCP emerges between C2 and C23 at the TS, but in addition, a new one occurs between H21 and H14, in agreement with the weak interaction region (green isosurface in Fig. 7E) probably involved in maintaining an optimum geometry for bonding interaction.

Finally, RDG analysis for the spin adduct $\cdot DMPO-CH_3$ (Fig. 7F) reveals three weak interaction zones (green-brown light isosurfaces) and a steric region (red isosurface) in the ring center, but additional critical points (besides those related with the intrinsic structure) were not found.

3.2.4. Spin density and ECDA for charge-transfer

At the beginning of the reaction, the spin density is mainly localized on $\cdot CH_3$, and particularly through p_i orbitals on C23 (isosurface in Fig. 8D). Subsequently, insofar that the reactants achieve the TS, the spin density on $\cdot CH_3$ starts to be reduced

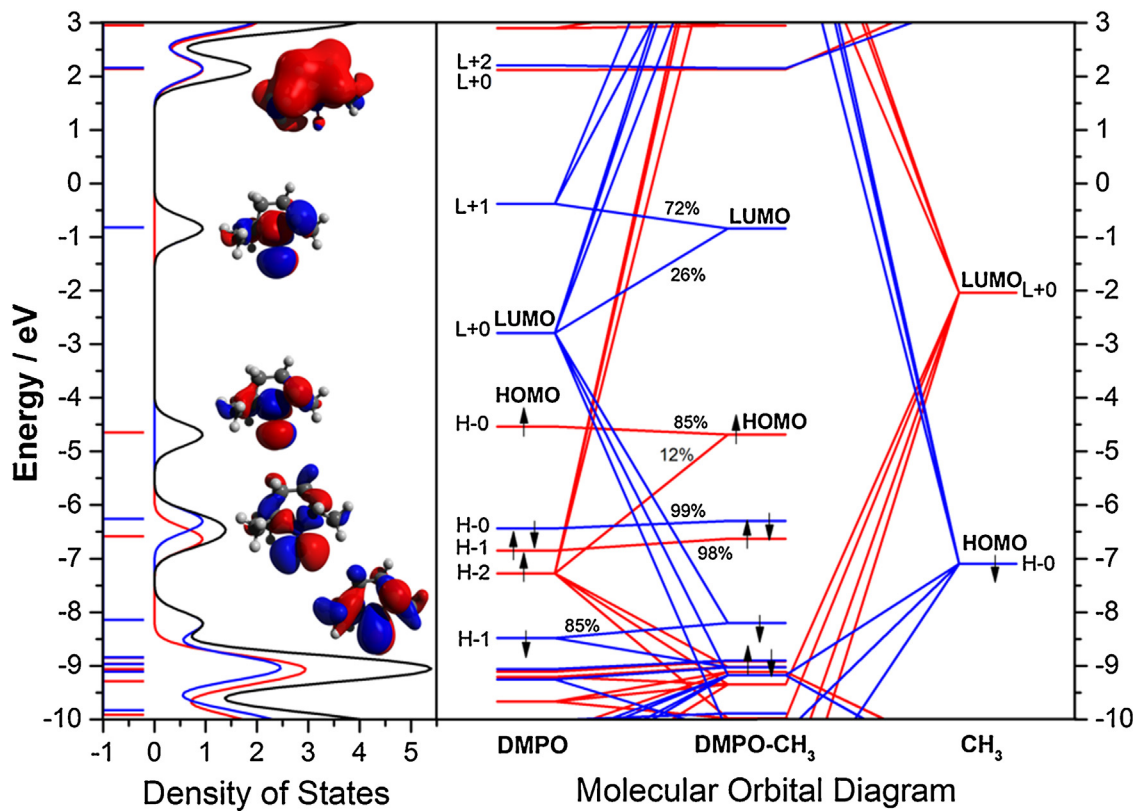


Fig. 13. Orbital interaction diagram (right) and density of state plot (left) for the spin-adduct $\cdot\text{DMPO-CH}_3$. At the right side, α - and β -spin orbitals are shown as red and blue lines, respectively. Connecting lines for contributions higher than 4% are included in the MO diagram. At the left, total (black), α (red) and β (blue) density of states (scaled by 1/2). The spin orbitals (α and β) have been exchanged (swapped) for the fragment $\cdot\text{CH}_3$. Selected MO isosurfaces were included to an isovalue of ± 0.02 . (For interpretation of the references to color in this text, the reader is referred to the web version of the article.)

(Fig. 9C) to such a degree that when the TS is reached, α spin density on C23 is significantly diminished, while on DMPO, both α (mainly on N1 and O6, and slightly on H15) as well as β (on C2) spin densities are increased (Figs. 8E and 9C,D). Thus, the α spin density regions on C23 are oriented toward those with β character on C2, which suggests that the binding could be also concerted through the pairing of these α - β spin regions. Additionally, Mulliken bond order analysis (MBOA) between C23 \cdots C2 yields a total bond order of $0.1968e^-$ given mainly by the orbitals $[\text{H-0}(\beta)]_{\text{TS}} \neq (0.1127e^-)$ and $[\text{H-2}(\alpha)]_{\text{TS}} \neq (0.1176e^-)$, and whose bonding character is clearly evidenced by their isosurfaces (see Fig. 5B). However, the BO predicted by Mulliken's partition is a bit far from what would be expected for the TS, instead, fuzzy bond order analysis [42] yields a total bond order of $0.4545e^-$, wherein α and β contributions are 0.2480 and $0.2064e^-$, respectively, in which, the major contributions can be safely associated to the aforementioned orbitals $[\text{H-2}(\alpha)]_{\text{TS}} \neq$ and $[\text{H-0}(\beta)]_{\text{TS}} \neq$, but with more meaningful values than those predicted by MBOA.

Continuing with the TS, ECDA reveals a small polarization of the DMPO's alpha orbitals ($[\text{PL}(\text{DMPO})]_\alpha \neq -[\text{PL}(\cdot\text{CH}_3)]_\alpha \neq = 0.0612$), and a significant α -spin electron donation from $\cdot\text{CH}_3$ to DMPO ($[\text{CT}(\text{DMPO} \rightarrow \cdot\text{CH}_3)]_\alpha \neq -[\text{CT}(\cdot\text{CH}_3 \rightarrow \text{DMPO})]_\alpha \neq = -0.1243$). On the contrary, beta electrons are transferred from DMPO to $\cdot\text{CH}_3$ ($[\text{CT}(\text{DMPO} \rightarrow \cdot\text{CH}_3)]_\beta \neq -[\text{CT}(\cdot\text{CH}_3 \rightarrow \text{DMPO})]_\beta \neq = 0.1600$) and accompanied by a small polarization term in $\cdot\text{CH}_3$ ($[\text{PL}(\text{DMPO})]_\beta - [\text{PL}(\cdot\text{CH}_3)]_\beta = -0.0406$). Thus, the net electron transfer goes from DMPO to $\cdot\text{CH}_3$ in the TS ($[\text{CT}(\text{DMPO} \rightarrow \cdot\text{CH}_3)]_{(\alpha+\beta)} \neq -[\text{CT}(\cdot\text{CH}_3 \rightarrow \text{DMPO})]_{(\alpha+\beta)} \neq = 0.0358$). Unsurprisingly, the net charge transferred is smaller than the predicted for the TS $\cdot[\text{DMPO}\cdots\text{OH}]^\neq$, which is by one hand, in

agreement with the precepts of electronegativity, but on the other hand, disclosing that this "small value" does not mean that a small electron transfer is occurring, instead, it rather reflects the compensation of α and β electrons which are transferred between the fragments constituting the TS.

Afterwards, to the extent that the TS becomes the spin-adduct (Fig. 8F), the spin density decreases both in C23(α) as well as in C2(β), while those of N1(α), O6(α) and H15(α) are increased in a similar fashion to that described for $\cdot\text{DMPO-OH}$. However, HFCCs for $\cdot\text{DMPO-CH}_3$ resulted in better agreement with the experimental values (see Table 2), which is also well-reflected by the spin densities values along the bond C2–H15 (Fig. 9D), in a much wider range than the observed for $\cdot\text{DMPO-OH}$. Thus, the described path for the spin density is in complete agreement with the OM interaction afore described, also, in complete agreement with the experimental comparison parameter, the HFCCs (see Table 2).

4. Discussion

According to the theoretical results, depending on the radical that is being trapped, two slightly different trapping pathways are found. For the trapping of $\cdot\text{OH}$, the beginning of the reaction is ruled by a strong H-bond interaction between H21 \cdots O6, while for $\cdot\text{CH}_3$, a significant MO interaction is observed. Thus, to the extent that the reactants reach the transition structure, a small narrowing in HOMO-LUMO gap of DMPO is observed, and a stronger cross-linking interaction between both fragments occurs. However, this process befalls mainly due to a proper orbital alignment, and whose interaction is helped by the "strong enough" weak interactions, thereby maximizing the orbital

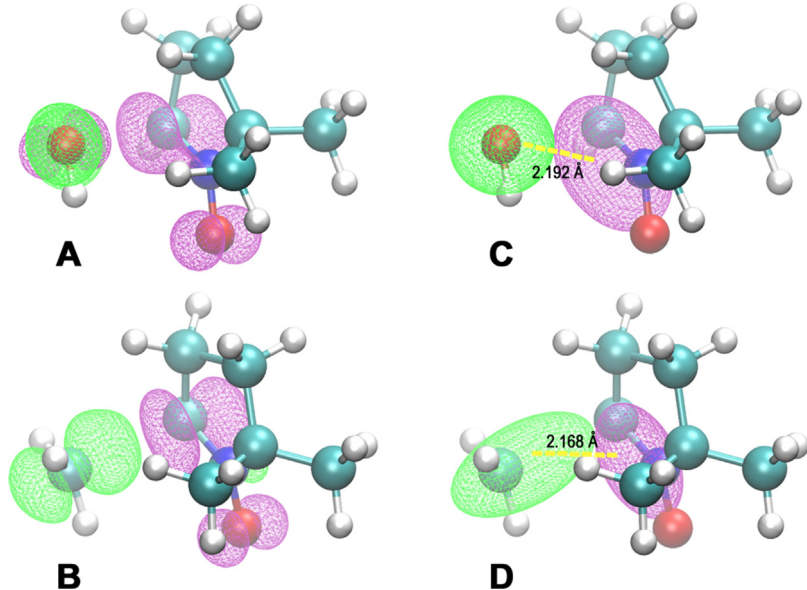


Fig. 14. Electron density variations through intrinsic differences and barycenters. At the left (A and B), isosurfaces for the difference in electron density between the transition complexes less the constituent fragments. The regions were filled with green and purple colors thereby reflecting the zones where the electron density is increased and reduced, respectively. At the right (C and D), plot of the isosurfaces for the functions $C_+(r)$ and $C_-(r)$, and whose regions were filled with green and purple color, respectively. The distance between the positive and negative barycenter is indicated for both transition structures. Notice that the charge transfer distance for $\cdot\text{CH}_3$ is smaller than that of $\cdot\text{OH}$. Isovalues for $\cdot[\text{DMPO}\cdots\text{OH}]^\pm$ and $\cdot[\text{DMPO}\cdots\text{CH}_3]^\pm$ were ± 0.006 and ± 0.003 , respectively. (For interpretation of the references to color in this text, the reader is referred to the web version of the article.)

intercrossing and charge transfer processes. Thus, when the TS is achieved, both for the trapping of $\cdot\text{OH}$ and $\cdot\text{CH}_3$, the formation of an antibonding orbital $[\text{HOMO-0}(\alpha)]^\pm$ responsible for hosting the unpaired electron is always observed (hereafter, when necessary, orbital subscripts will be included for readability). However, by the fact that the allowed combinations are controlled by the spin-orbital, $\cdot\text{CH}_3$ interacts with $[\text{HOMO-0}(\alpha)]^\pm$ through the highest occupied MO $[\text{HOMO-0}(\alpha)]_{\text{CH}_3}^\pm$, while $\cdot\text{OH}$ does so by $[\text{H-0}(\alpha)]_{\text{OH}}^\pm$ (because the highest occupied orbital has β spin), which renders the contributions from $\cdot\text{OH}$ to $[\text{HOMO-0}(\alpha)]_{\text{DMPO-OH}}^\pm$ are smaller than those of $\cdot\text{CH}_3$ to $[\text{HOMO-0}(\alpha)]_{\text{DMPO-CH}_3}^\pm$.

Regarding the binding interaction, two main bonding orbitals were clearly identified and referred in Fig. 5 as $[\text{H-1}(\beta)]^\pm$ and $[\text{H-3}(\alpha)]^\pm$ for $\cdot[\text{DMPO}\cdots\text{OH}]^\pm$, as well as $[\text{H-0}(\beta)]^\pm$ and $[\text{H-2}(\alpha)]^\pm$ for $\cdot[\text{DMPO}\cdots\text{CH}_3]^\pm$. However, the contributing fragment orbitals differ from each other. Thus, both for $[\text{H-0}(\beta)]_{\text{DMPO-CH}_3}^\pm$ and $[\text{H-1}(\beta)]_{\text{DMPO-OH}}^\pm$, the major contributions come from DMPO through $[\text{HOMO-0}(\alpha,\beta)]^\pm$, but the counterparts are given by $[\text{HOMO-0}(\beta)]_{\text{OH}}^\pm$ and $[\text{LUMO-0}(\beta)]_{\text{OH}}^\pm$, while $\cdot\text{CH}_3$ does so from $[\text{LUMO-0}(\beta)]_{\text{CH}_3}^\pm$, respectively. Contrariwise, $[\text{H-3}(\alpha)]_{\text{DMPO-OH}}^\pm$ and $[\text{H-2}(\alpha)]_{\text{DMPO-CH}_3}^\pm$ are mainly constituted by $[\text{H-0}(\alpha)]_{\text{OH}}^\pm$ and $[\text{HOMO-0}(\alpha,\beta)]_{\text{DMPO}}^\pm$, respectively.

In view of the discussion above, the role of the unpaired electron in $\cdot\text{OH}$ and $\cdot\text{CH}_3$ is somehow different for the trapping reactions here studied; in the first case, it is clearly involved in one of the bonding interactions $[\text{H-1}(\beta)]_{\text{DMPO-OH}}^\pm$, while in the second one, it is related to one of the bonding interactions $[\text{H-2}(\alpha)]_{\text{DMPO-CH}_3}^\pm$, as well as in the formation of the antibonding orbital responsible for hosting the unpaired electron $[\text{HOMO-0}(\alpha)]_{\text{DMPO-CH}_3}^\pm$.

For the spin-adducts, the scenario is completely different between both systems. Thus, for $\cdot\text{DMPO-OH}$, both $\text{HOMO-0}(\alpha)_{\text{DMPO-OH}}$ as $\text{LUMO-0}(\beta)_{\text{DMPO-OH}}$ are mainly constituted by the combination between $\text{HOMO-0}(\alpha,\beta)_{\text{DMPO}}$ and $\text{LUMO-0}(\alpha,\beta)_{\text{DMPO}}$ through contributions close to 50% by each. Contrariwise, for $\cdot\text{DMPO-CH}_3$, $\text{HOMO}(\alpha)_{\text{DMPO-CH}_3}$ and $\text{LUMO}(\beta)_{\text{DMPO-CH}_3}$ are

exclusively constituted by the combination of occupied ($\text{H-0}(\alpha)_{\text{DMPO}}$ and $\text{H-1}(\alpha)_{\text{DMPO}}$) and unoccupied ($\text{L+0}(\beta)_{\text{DMPO}}$ (26%) and $\text{L+1}(\beta)_{\text{DMPO}}$) orbitals, respectively. Therefore, unlike $\cdot\text{DMPO-OH}$, the adduct $\cdot\text{DMPO-CH}_3$ does not display cross-link connections with HOMO-LUMO orbitals of DMPO, which suggests that inaccuracies in the prediction of the HFCCs for $\cdot\text{DMPO-OH}$ are due to a miscalculation into the contributions of the combined orbitals that give rise to $\text{HOMO-0}(\alpha)_{\text{DMPO-OH}}$ and $\text{LUMO-0}(\beta)_{\text{DMPO-OH}}$; most likely, because the resultant structure is not accurate enough to achieve a global minimum, which in turn would explain why the spin densities remain almost unaffected to the extent that TS becomes $\cdot\text{DMPO-OH}$. On the contrary, for the spin-adduct $\cdot\text{DMPO-CH}_3$, calculated HFCCs match completely with the experimental results because, unlike $\cdot\text{DMPO-OH}$, there is no significant interaction between occupied and unoccupied orbitals of DMPO. Instead, the final configuration is given by the splitting into the α,β orbitals of DMPO, conducive to the interaction of, by one hand, single occupied orbitals, and on the other hand, single unoccupied orbitals as it was exemplified for $\text{HOMO-0}(\alpha)_{\text{DMPO-CH}_3}$ and $\text{LUMO-0}(\beta)_{\text{DMPO-CH}_3}$.

On the other hand, the charge transfer analysis has been focused on the transition structures (of course, the spotlight on this study). Thus, ECDA revealed that, in $\cdot[\text{DMPO}\cdots\text{OH}]^\pm$, the charge is transferred primarily from DMPO to $\cdot\text{OH}$ through β orbitals, which is in turn accompanied by a strong electron polarization term in $\cdot\text{OH}$, indeed, in agreement with the rearrangement of the electron density necessary for the redistribution of the charge that is transferred to this fragment. For $\cdot[\text{DMPO}\cdots\text{CH}_3]^\pm$, instead, the charge transfer occurs in both directions, so that DMPO behaves like an α -acceptor/ β -donor, while $\cdot\text{CH}_3$ as a β -acceptor/ α -donor. However, even though the ECDA method provides a proper reading of the charge transfer, the visual inspection is helpful to obtain a better understanding of the phenomenon. Thus, when plotting the isosurfaces for the electron density variation (for the complex minus the constituent fragments), the image that is obtained (Fig. 14A and B) is somehow difficult to be interpreted because

it is not intuitive, positive and negative parts are intertwined together.

However, Le Bahers et al. [35] proposed a method for analyzing charge-transfer (CT) during electron transition through the electron density variations between excited (EX) and ground state (GS) based on $\Delta\rho(\mathbf{r}) = \rho_{\text{EX}}(\mathbf{r}) - \rho_{\text{GS}}(\mathbf{r})$, in which $\rho_i(\mathbf{r})$ can be split into positive and negative parts $\rho_+(\mathbf{r})$ and $\rho_-(\mathbf{r})$, and whose integral correspond to the transferred charge. Thus, in order to get a more intuitive picture of the charge transfer, two centroids of charge ($C_+(\mathbf{r})$ and $C_-(\mathbf{r})$) associated with the negative and positive regions have been defined and normalized with the constrain that the integrated charge on the centroid to be equal to the corresponding density change integrated in the whole space (see the referred paper for mathematical details). Although the original article focuses on the one dimensional case, Multiwfn software implements the generalized scheme for three-dimensions cases [36], and consequently, the original model can be safely extrapolated to any i state along the trapping reactions as $\Delta\rho_i(\mathbf{r}) = \rho_{i,\text{complex}}(\mathbf{r}) - \sum \rho_{i,\text{fragment}}(\mathbf{r})$.

Thus, using this method on the TS's $^{\bullet}[\text{DMPO}\cdots\text{OH}]^\neq$ and $^{\bullet}[\text{DMPO}\cdots\text{CH}_3]^\neq$, the isosurfaces for $C_+(\mathbf{r})$ and $C_-(\mathbf{r})$ (Fig. 14C and D) indicate that, in both cases, the negative barycenter is centered close to the bond N1 \cdots C2 suggesting that the charge transferred from DMPO is extracted at the expense of the π cloud to then be transferred to the corresponding positive barycenter. In the same vain, however, the positive centroid is positioned on different coordinates in both structures. Thus, for $^{\bullet}[\text{DMPO}\cdots\text{OH}]^\neq$, the positive barycenter is situated on O20 (Fig. 14C) and distributed in perpendicular shape to the charge transfer direction, confirming again that the charge transfer occurs from DMPO to $^{\bullet}\text{OH}$, but in addition, that the extracted charge is going to be redistributed mainly on O20, a logical outcome from the simplest idea of electronegativity. However, the positive barycenter for $^{\bullet}[\text{DMPO}\cdots\text{CH}_3]^\neq$ takes place between C2 and C23 (Fig. 14D), which is not only in agreement with the fact that $^{\bullet}\text{CH}_3$ will exhibit a net gain in electron density (ECDA result), but also, with the fact that the charge transferred by DMPO is being redistributed on what will be the bond between C2 and C23, and only a part of this is going to be assigned on C23, evidently, in complete agreement with the small value of charge transfer predicted by ECDA, of course, because it is not going to be totally allocated on $^{\bullet}\text{CH}_3$ but mainly along the bond that is about to be formed between C23 and C2. Thus, Le Bahers' method proved to be a very helpful tool for understanding the charge transfer phenomena, because in it, unlike ECDA, the transferred charge is defined by the integration, over all space, of the increments and depletions negative zones in electron density variations, and centered on positive and negative barycenters, respectively.

5. Conclusions

Attempts to locate the TS for the trapping reaction of $^{\bullet}\text{OH}$ by DMPO have been unsuccessful so far. It has even been postulated the nonexistence of TS due to a strong endothermic formation of the product [9]. However, a breakthrough in this task has been achieved here, and the TS's for the trapping reactions of $^{\bullet}\text{OH}$ and $^{\bullet}\text{CH}_3$ by DMPO have been described along the intrinsic reaction coordinate. In addition, due to the lack of information about the factors that govern the reaction pathway, an extensive analysis on the MO interactions was performed on three of the essential states along the reaction (reactants, TS and product), from which, more than a few significant differences for each reaction were disclosed, among these, the orbitals (and nature thereof) involved in bonding and antibonding interactions, as well as the contributions of DMPO and its influence on the hyperfine coupling constants are some of those found. On the other hand, RDG analysis revealed the relevance of weak interactions

in the pathway, mainly at the beginning of the reaction as well as at the transition state, while ECDA combined with barycenter analysis of charge transfer revealed a different transfer mechanism for each trapping reaction. Thus, the description provided here was in good agreement with the used comparison parameter (HFCC), evidently, some differences between calculated and experimental HFCCs for $^{\bullet}\text{DMPO-OH}$ were found, however, for the spin-adduct $^{\bullet}\text{DMPO-CH}_3$, a better agreement was achieved. Additionally, when compares free energy values with previous reports, our model of $^{\bullet}\text{DMPO-OH}$ was closer to that predicted in previous reports (see Table 1), while the model of $^{\bullet}\text{DMPO-CH}_3$, free energy predictions were not resulted in agreement with previous reports, probably, due to conformational differences between the theoretical models (see Refs. [9–11] for details on this issue). Interestingly, the model of $^{\bullet}\text{DMPO-OH}$ does not reproduce accurately the HFCC, but it is in agreement with previous free energy predictions, and on the other hand, $^{\bullet}\text{DMPO-CH}_3$ gives accurate HFCC values, but it does not agree with previous free energy predictions.

On the other hand, it is clearly revealed the reliability of the Mulliken partition model for reactions such as the trapping of methyl radical (and with some confidence extendable to the trapping of carbon-centered radicals), but questionable for trapping of highly electronegative radicals such $^{\bullet}\text{OH}$. However, along the reaction, the models were comparable at all except for the spin adducts, and the goal has been successfully accomplished. Now, there just remains to take the next step forward for improving this model, but the hardest part is done, and the molecular orbital models for the trapping of $^{\bullet}\text{CH}_3$ and $^{\bullet}\text{OH}$ (the latter, the most urgent for sure) are now available.

To conclude, we like to caution on the need for future research to complement this study, because, despite having provided an accurate enough description to understand the molecular trapping mechanisms, an upgraded and comprehensive kinetic study is the next step to be followed in the way to finally complete the reaction mechanism profiles for $^{\bullet}\text{DMPO-OH}$ and $^{\bullet}\text{DMPO-CH}_3$.

Acknowledgement

This research was supported by FONDECYT Postdoctorado 3130364.

Appendix A. Supplementary data

Supplementary data associated with this article can be found, in the online version, at <http://dx.doi.org/10.1016/j.jmgm.2014.06.006>.

References

- [1] J.D. Maya, C.O. Salas, B. Aguilera-Venegas, M.V. Díaz, R. López-Munoz, Key proteins in the polyamine-trypanothione pathway as drug targets against *Trypanosoma cruzi*, *Curr. Med. Chem.* 21 (2014) 1757–1771.
- [2] V. Sosa, T. Moliné, R. Somoza, R. Paciucci, H. Kondoh, M.E. Leonart, Oxidative stress and cancer: an overview, *Ageing Res. Rev.* 12 (2013) 376–390.
- [3] G.R. Buettner, R.P. Mason, Spin-trapping methods for detecting superoxide and hydroxyl free radicals *in vitro* and *in vivo*, in: A.N.G. Lester Packer (Ed.), *Methods in Enzymology*, vol. 186, Academic Press, 1990, pp. 127–133, [http://dx.doi.org/10.1016/0076-6879\(90\)86101-Z](http://dx.doi.org/10.1016/0076-6879(90)86101-Z), PMID: 2172700.
- [4] B. Aguilera-Venegas, C. Olea-Azar, V.J. Arán, H. Speisky, Indazoles: a new top seed structure in the search of efficient drugs against *Trypanosoma cruzi*, *Future Med. Chem.* 5 (2013) 1843–1859.
- [5] M. Kohno, Applications of electron spin resonance spectrometry for reactive oxygen species and reactive nitrogen species research, *J. Clin. Biochem. Nutr.* 47 (2010) 1–11.
- [6] G. Barriga-González, B. Aguilera-Venegas, C. Folch-Cano, F. Pérez-Cruz, C. Olea-Azar, Electron spin resonance as a powerful tool for studying antioxidants and radicals, *Curr. Med. Chem.* 20 (2013) 4731–4743.

- [7] F.A. Villamena, J.K. Merle, C.M. Hadad, J.L. Zweier, Superoxide radical anion adduct of 5,5-dimethyl-1-pyrroline N-oxide (DMPO). 1. The thermodynamics of formation and its acidity, *J. Phys. Chem. A* 109 (2005) 6083–6088.
- [8] E.J. Locigno, J.L. Zweier, F.A. Villamena, Nitric oxide release from the unimolecular decomposition of the superoxide radical anion adduct of cyclic nitrones in aqueous medium, *Org. Biomol. Chem.* 3 (2005) 3220–3227.
- [9] F.A. Villamena, A. Rockenbauer, J. Gallucci, M. Velayutham, C.M. Hadad, J.L. Zweier, Spin trapping by 5-carbamoyl-5-methyl-1-pyrroline N-oxide (AMPO): theoretical and experimental studies, *J. Org. Chem.* 69 (2004) 7994–8004.
- [10] F.A. Villamena, C.M. Hadad, J.L. Zweier, Comparative DFT study of the spin trapping of methyl, mercapto, hydroperoxy, superoxide, and nitric oxide radicals by various substituted cyclic nitrones, *J. Phys. Chem. A* 109 (2005) 1662–1674.
- [11] F.A. Villamena, S. Xia, J.K. Merle, R. Lauricella, B. Tuccio, C.M. Hadad, et al., Reactivity of superoxide radical anion with cyclic nitrones: role of intramolecular H-bond and electrostatic effects, *J. Am. Chem. Soc.* 129 (2007) 8177–8191.
- [12] B. Aguilera-Venegas, C. Olea-Azar, V.J. Arán, J.D. Maya, U. Kemmerling, H. Speisky, et al., Electrochemical, ESR and theoretical insights into the free radical generation by 1,1'-hydrocarbylenebisindazoles and its evaluation as potential bio-active compounds, *Int. J. Electrochem. Sci.* 7 (2012) 5837–5863.
- [13] E.R. Johnson, S. Keinan, P. Mori-Sánchez, J. Contreras-García, A.J. Cohen, W. Yang, Revealing noncovalent interactions, *J. Am. Chem. Soc.* 132 (2010) 6498–6506.
- [14] R.F.W. Bader, T.T. Nguyen-Dang, Quantum theory of atoms in molecules – Dalton revisited, in: L. Per-Olov (Ed.), *Advances in Quantum Chemistry*, vol. 14, Academic Press, 1981, pp. 63–124, [http://dx.doi.org/10.1016/S0065-3276\(08\)60326-3](http://dx.doi.org/10.1016/S0065-3276(08)60326-3).
- [15] G. Saleh, C. Gatti, L. Lo Presti, Non-covalent interaction via the reduced density gradient: independent atom model vs experimental multipolar electron densities, *Comput. Theor. Chem.* 998 (2012) 148–163.
- [16] M.J. Frisch, G.W. Trucks, H.B. Schlegel, G.E. Scuseria, M.A. Robb, J.R. Cheeseman, et al., Gaussian 09, Revision B.01, Gaussian, Inc., Wallingford, CT, 2010.
- [17] C. Peng, P.Y. Ayala, H.B. Schlegel, M.J. Frisch, Using redundant internal coordinates to optimize equilibrium geometries and transition states, *J. Comput. Chem.* 17 (1996) 49–56.
- [18] C. Lee, W. Yang, R.G. Parr, Development of the Colle-Salvetti correlation-energy formula into a functional of the electron density, *Phys. Rev. B* 37 (1988) 785–789.
- [19] A.D. Becke, Density-functional thermochemistry. III. The role of exact exchange, *J. Chem. Phys.* 98 (1993) 5648–5652.
- [20] G. Scalmani, M.J. Frisch, Continuous surface charge polarizable continuum models of solvation. I. General formalism, *J. Chem. Phys.* 132 (2010) 114110.
- [21] F.A. Villamena, M.H. Dickman, D.R. Crist, Nitrones as ligands in complexes of Cu(II), Mn(II), Co(II), Ni(II), Fe(II), and Fe(III) with N-tert-butyl- α -(2-pyridyl)nitrone and 2,5,5-trimethyl-1-pyrroline-N-oxide†, *Inorg. Chem.* 37 (1998) 1446–1453.
- [22] Y.-K. Xu, Z.-W. Chen, J. Sun, K. Liu, W. Chen, W. Shi, et al., Synthesis, crystal structure, and ESR study of a novel phosphorylated lipophilic spin trap, *J. Org. Chem.* 67 (2002) 7624–7630.
- [23] J.C.A. Boeyens, G.J. Kruger, Remeasurements of the structure of potassium-2,2,5,5-tetramethyl-3-carboxypyrroline-1-oxyl, *Acta Crystallogr. B* 26 (1970) 668–672.
- [24] Y. Lin, H. Wang, S. Gao, R. Li, H.F. Schaefer, Hydrogen-bonded double-proton transfer in five guanine–cytosine base pairs after hydrogen atom addition, *J. Phys. Chem. B* 116 (2012) 8908–8915.
- [25] B. Aguilera-Venegas, C. Olea-Azar, E. Norambuena, V.J. Arán, F. Mendizábal, M. Lapier, et al., ESR, electrochemical, molecular modeling and biological evaluation of 4-substituted and 1,4-disubstituted 7-nitroquinoxalin-2-ones as potential anti-*Trypanosoma cruzi* agents, *Spectrochim. Acta A: Mol. Biomol. Spectrosc.* 78 (2011) 1004–1012.
- [26] K. Kitaura, K. Morokuma, A new energy decomposition scheme for molecular interactions within the Hartree-Fock approximation, *Int. J. Quantum Chem.* 10 (1976) 325–340.
- [27] T. Ziegler, A. Rauk, On the calculation of bonding energies by the Hartree Fock Slater method, *Theor. Chim. Acta* 46 (1977) 1–10.
- [28] S. Dapprich, G. Frenking, Investigation of donor–acceptor interactions: a charge decomposition analysis using fragment molecular orbitals, *J. Phys. Chem.* 99 (1995) 9352–9362.
- [29] G. Frenking, N. Fröhlich, The nature of the bonding in transition-metal compounds, *Chem. Rev.* 100 (2000) 717–774.
- [30] S.I. Gorelsky, E.I. Solomon, Extended charge decomposition analysis and its application for the investigation of electronic relaxation, *Theor. Chem. Acc.* 119 (2008) 57–65.
- [31] S.I. Gorelsky, S. Ghosh, E.I. Solomon, Mechanism of N₂O reduction by the μ 4-S tetrานuclear CuZ cluster of nitrous oxide reductase, *J. Am. Chem. Soc.* 128 (2006) 278–290.
- [32] S.I. Gorelsky, AOMix Program for Molecular Orbital Analysis, University of Ottawa, 2010 <http://www.sg-chem.net/>
- [33] A.E. Reed, R.B. Weinstock, F. Weinhold, Natural population analysis, *J. Chem. Phys.* 83 (1985) 735–746.
- [34] E.D. Glendening, J.K. Badenhoop, A.E. Reed, J.E. Carpenter, J.A. Bohmann, C.M. Morales, et al., NBO 5.6 www.chem.wisc.edu/~nbo5, Theoretical Chemistry Institute, University of Wisconsin, Madison, WI, 2001.
- [35] T. Le Bahers, C. Adamo, I. Ciofini, A qualitative index of spatial extent in charge-transfer excitations, *J. Chem. Theory Comput.* 7 (2011) 2498–2506.
- [36] T. Lu, C.F. Multiwfns, A multifunctional wavefunction analyzer, *J. Comput. Chem.* 33 (2012) 580–592.
- [37] M. Hanwell, D. Curtis, D. Lonie, T. Vandermeersch, E. Zurek, G. Hutchison, Avogadro: an advanced semantic chemical editor, visualization, and analysis platform, *J. Cheminform.* 4 (2012) 17.
- [38] W. Humphrey, A. Dalke, K.V.M.D. Schulten, Visual molecular dynamics, *J. Mol. Graph.* 14 (1996) 33–38.
- [39] Persistence of Vision Raytracer, Persistence of Vision Pty. Ltd., Williamstown, Victoria, Australia, 2004.
- [40] E. Espinosa, E. Molins, C. Lecomte, Hydrogen bond strengths revealed by topological analyses of experimentally observed electron densities, *Chem. Phys. Lett.* 285 (1998) 170–173.
- [41] R. Parthasarathi, V. Subramanian, N. Sathyamurthy, Hydrogen bonding without borders: an atoms-in-molecules perspective, *J. Phys. Chem. A* 110 (2006) 3349–3351.
- [42] I. Mayer, P. Salvador, Overlap populations, bond orders and valences for ‘fuzzy’ atoms, *Chem. Phys. Lett.* 383 (2004) 368–375.